### **OPEN ACCESS**



# Observations of Magnetic Reconnection and Particle Acceleration Locations in Solar Coronal Jets

Yixian Zhang <sup>1</sup> , Sophie Musset <sup>2</sup> , Lindsay Glesener <sup>1</sup> , Navdeep K. Panesar <sup>3,4</sup> , and Gregory D. Fleishman <sup>5</sup> 
School of Physics and Astronomy, University of Minnesota, 116 Church Street SE, Minneapolis, MN 55455, USA; zhan6327@umn.edu 
European Space Agency (ESA), European Space Research and Technology Centre (ESTEC), Keplerlaan 1, 2201 AZ, Noordwijk, The Netherlands 
Lockheed Martin Solar and Astrophysics Laboratory, 3251 Hanover Street, Building 252, Palo Alto, CA 94304, USA 

Bay Area Environmental Research Institute, NASA Research Park, Moffett Field, CA 94035, USA 
Center For Solar-Terrestrial Research, New Jersey Institute of Technology, Newark, NJ 07102, USA 
Received 2022 June 29; revised 2022 November 23; accepted 2022 November 24; published 2023 February 7

#### **Abstract**

We present a multiwavelength analysis of two flare-related jets on 2014 November 13, using data from the Solar Dynamics Observatory/Atmospheric Imaging Assembly (SDO/AIA), the Reuven High Energy Solar Spectroscopic Imager (RHESSI), the Hinode/X-ray Telescope (XRT), and the Interface Region Imaging Spectrograph (IRIS). Unlike most coronal jets, where hard X-ray (HXR) emissions are usually observed near the jet base, in these events HXR emissions are found at several locations, including in the corona. We carry out the first differential emission measure analysis that combines both AIA (and XRT, when available) bandpass filter data and RHESSI HXR measurements for coronal jets, and obtain self-consistent results across a wide temperature range and into nonthermal energies. In both events, hot plasma first appears at the jet base, but as the base plasma gradually cools, hot plasma also appears near the jet top. Moreover, nonthermal electrons, while only mildly energetic, are found in multiple HXR locations and contain large amounts of total energy. In particular, the energetic electrons that produce the HXR sources at the jet top are accelerated near the top location, rather than traveling from a reconnection site at the jet base. This means that there is more than one particle acceleration site in each event. Jet velocities are consistent with previous studies, including the upward and downward velocities around  $\sim$ 200 km s<sup>-1</sup> and  $\sim$ 100 km s<sup>-1</sup>, respectively, and fast outflows of 400–700 km s<sup>-1</sup>. We also examine the energy partition in the later event, and find that the nonthermal energy in the accelerated electrons is most significant compared to the other energy forms considered. We discuss the interpretations and provide constraints on the mechanisms for coronal jet formation.

Unified Astronomy Thesaurus concepts: The Sun (1693); Solar x-ray flares (1816); Solar energetic particles (1491); Jets (870)

Supporting material: animations

### 1. Introduction

Solar coronal jets are collimated plasma ejections that occur in the solar corona and they offer ways for plasma and particles to enter interplanetary space. They are transient (lasting tens of minutes), but ubiquitous, with a typical height of  $\sim 5 \times 10^4$  km and a typical width of  $\sim 8 \times 10^3$  km (e.g., Savcheva et al. 2007). X-ray emissions from coronal jets were first observed by the Soft X-ray Telescope on board Yohkoh in the early 1990s (Shibata et al. 1992). Since then, various aspects of coronal jets have been studied, including their morphology, dynamics, driving mechanisms, and more (see, e.g., Raouafi et al. 2016; Shen 2021). Jets or jet-like events have also been observed in other wavelengths, such as extreme ultraviolet (EUV), ultraviolet (UV), and H alpha (those studied in H alpha are historically known as "surges"; e.g., Innes et al. 1997; Chae et al. 1999; Nistico et al. 2009). These wavebands cover a wide range of plasma temperatures (from chromospheric to coronal), and one important feature of jets is the presence of both hot and cool components in many events (Moore et al. 2010, 2013).

Current models generally suggest that jets are formed by magnetic reconnection between open and closed magnetic field

Original content from this work may be used under the terms of the Creative Commons Attribution 4.0 licence. Any further distribution of this work must maintain attribution to the author(s) and the title of the work, journal citation and DOI.

lines; however, the detailed triggering process for such magnetic reconnection is still not fully clear. In the emerging flux model, jets are generated through interchange reconnection when the field lines of the newly emerging magnetic flux reach those of the preexisting open field (Shibata et al. 1992). As shown in the 2D simulation by Yokoyama & Shibata (1995, 1996), this model could successfully produce a hot jet and an adjacent cool jet (or surge) simultaneously. The embedded-bipole model developed by Pariat et al. (2015, 2016, etc.) considers a 3D fan-spine topology, where magnetic reconnection occurs around the 3D null point. In their simulation, straight jets are generated through slow reconnection at the current sheet and driven by magnetic tension, while helical jets are generated through explosive magnetic reconnection that is triggered by a kink-like instability and driven by a rapid untwisting process of the magnetic field lines. Recently, a few studies have reported small-scale filament structures (known as "minifilaments") at the base of some coronal jets, leading to the minifilament eruption model (Sterling et al. 2015; Panesar et al. 2016b; Sterling et al. 2016; Panesar et al. 2017; Wyper et al. 2017, 2018; Panesar et al. 2018; Moore et al. 2018; McGlasson et al. 2019). This model suggests that jets are generated through miniature filament eruptions similar to those that drive larger eruptive events, such as coronal mass ejections (CMEs). In addition to the external/interchange magnetic reconnection, this process also involves internal magnetic reconnection inside the filament-carrying field, and the jet bright point (JBP, which corresponds to the solar flare arcade in the larger-scale case) appears underneath the erupting minifilament. Many recent observations have shown that the triggers for these minifilament eruptions are usually magnetic flux cancellation (Hong et al. 2011; Huang et al. 2012; Adams et al. 2014; Panesar et al. 2016b, 2017, 2018; McGlasson et al. 2019; Muglach 2021).

Hard X-ray (HXR) observations can also provide helpful insights into jet formation mechanisms, by constraining the energetic electron populations within coronal jets. Krucker et al. (2011) investigated the HXR emissions for 16 flarerelated energetic electron events and found that seven of them showed three distinct HXR footpoints, consistent with the interchange reconnection geometry. (In the remaining events, the fact that they showed fewer than three sources was likely due to instrument limitations.) Also in that study, EUV jets were found in all six events that had EUV data coverage. HXR bremsstrahlung emissions could also directly come from coronal iets, if there are energetic electrons, but those extended sources are usually much fainter than the footpoint sources, and only a few studies (Bain & Fletcher 2009; Glesener et al. 2012) have reported such observations. More recently, Glesener & Fleishman (2018) combined HXR observations with microwave emission, EUV emission, and magnetogram data, performing 3D modeling of the electron distributions for a flare-related jet. They obtained direct constraints on the energetic electron populations within that event. Musset et al. (2020) carried out a statistical study of 33 flare-related coronal jets using HXR and EUV data, and they observed nonthermal emissions from energetic electrons in eight of these events. They also studied the relation between jets and the associated flares, but found no clear correlations between jet and flare properties.

In most of the previous studies of coronal jets, hot plasma and HXR emissions have been found near the base of the jet (the location of the primary reconnection site; e.g., Krucker et al. 2011; Mulay et al. 2016; Musset et al. 2020). However, for two coronal jets on 2014 November 13, HXR thermal emissions were observed near the far end of the jet spire (hereafter, the "top"). In fact, in the second event, which had full HXR coverage, HXR emissions were observed at three different locations: the base of the jet, the top of the jet, and a location to the north of the jet. Here, we present a multiwavelength analysis of these two jets using data from the Atmospheric Imaging Assembly (AIA) on board the Solar Dynamics Observatory (SDO), the Reuven High Energy Solar Spectroscopic Imager (RHESSI), the X-ray Telescope (XRT) on board Hinode, and the Interface Region Imaging Spectrograph (IRIS). We find that all these different HXR sources show evidence of mildly accelerated electrons, and that particle acceleration also occurred near the jet top, in addition to the site at the jet base. To our knowledge, this is the most thorough HXR study of particle acceleration in coronal jets

The paper is structured as follows. In Section 2, we describe the observations from each instrument. In Section 3, we show the results from differential emission measure (DEM) analysis, imaging spectroscopy, and velocity estimation. In Section 4, we calculate the energy budget for one of the jets, discuss the interpretations of the observational results, and compare them

with jet models. Finally, in Section 5, we summarize the key findings of this work.

#### 2. Observations

On 2014 November 13, more than 10 recurrent jets were ejected from NOAA Active Region 12209, near the eastern solar limb, at different times throughout the day. While most (if not all) of the jets can be identified in one or more AIA channels, only two events—SOL2014-11-13T17:20 and SOL2014-11-13T20:47—were simultaneously observed by AIA and RHESSI. We select these two flare-related jets for this study, and we add supporting observations from XRT and IRIS. The associated flares are GOES class C1.5–1.7, without background subtraction (see the top row of Figure 1), or B2.4–3.7, with background subtraction.

#### 2.1. AIA Data

The AIA instrument provides full-disk solar images in 10 EUV/UV/visible-light channels, with a spatial resolution of 1."5 (Lemen et al. 2012). In this work, we use data from the seven EUV channels of AIA: 94 Å, 131 Å, 171 Å, 193 Å, 211 Å, 304 Å, and 335 Å—which have a cadence of 12 s and cover plasma temperatures from  $\sim$ 0.05 MK up to  $\sim$ 20 MK.

Figures 2 and 3 show AIA images of the two jets in the 131 Å and 304 Å channels at selected times. At the beginning of each event, a minifilament—indicated by the yellow arrow in panel (k)—was identified in multiple AIA channels at the base of the jet. After the minifilament eruption, a JBP (indicated by the green arrows) appeared underneath the prior minifilament location.

Interestingly, both events showed slightly different jet evolutions in the cool and hot AIA channels. In the cooler channels, including 171 Å, 193 Å, 211 Å, 304 Å, and 335 Å, the first jet started at  $\sim$ 17:15 UT, reached its maximum extent at  $\sim$ 17:23 UT, and lasted about 20 minutes. However, in the hot channels that are sensitive to ≥10 MK plasma (94 Å and 131 Å, in particular), the jet reached its maximum height within five minutes of the same starting time; it then slightly expanded transversely, and gradually faded away over a much longer period of time. (The 193 Å channel, in principle, could also measure hot plasma (Lemen et al. 2012), but its response was dominated by temperatures below 10 MK, and thus it looked like a cool channel.) Similar behavior was observed in the later jet, which started at  $\sim$ 20:40 UT and reached its maximum extent at  $\sim$ 20:47 UT in the hotter 94 Å and 131 Å channels, and at  $\sim$ 20:50 UT in the rest of the channels. The jet had already disappeared in those cooler channels before 20:58 UT, but it was visible in 94 Å and 131 Å for more than an hour.

### 2.2. RHESSI Data

RHESSI was a solar-dedicated HXR observatory that was launched in 2002 and decommissioned in 2018. It consisted of nine rotating modulation collimators, each placed in front of a cooled germanium detector, and it used indirect Fourier imaging techniques. RHESSI measured both images and spectra over the full Sun in the energy range of  $3\,\mathrm{keV}{-}17\,\mathrm{MeV}$ , and it had good spatial and energy resolutions, especially for lower energies (2."3 and  $\sim$ 1 keV, respectively; Lin et al. 2002).

RHESSI was in eclipse during 16:46–17:23 UT, so it did not capture all of the first jet; but RHESSI did have full coverage

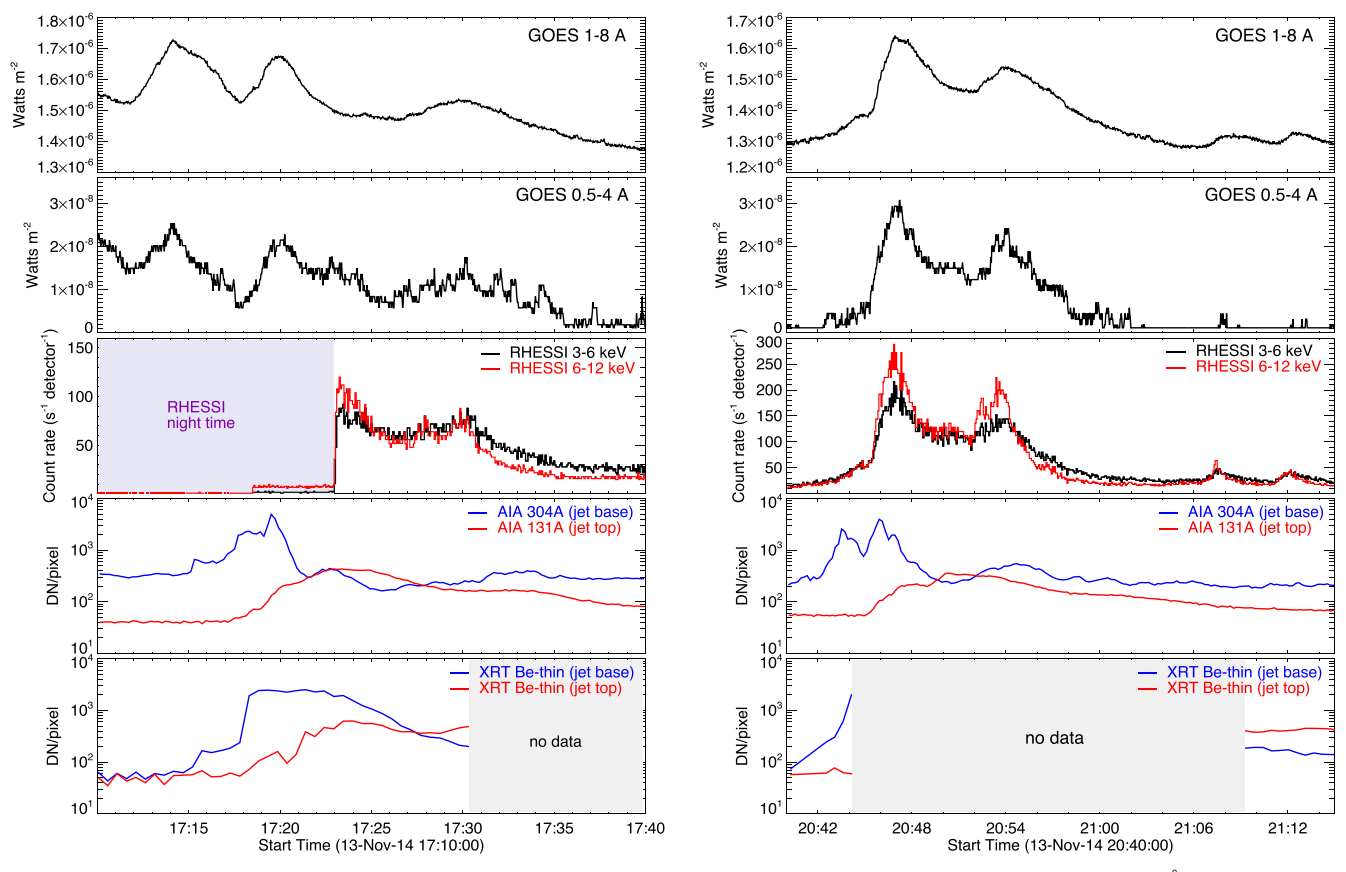


Figure 1. Time profiles of the  $\sim$ 17:20 jet (left) and the  $\sim$ 20:47 jet (right) on 2014 November 13. Top row: GOES light curves in the 1–8 Å channel. Second row: GOES light curves in the 0.5–4 Å channel. Third row: RHESSI emission in 3–6 keV (black) and 6–12 keV (red), using detectors 3, 6, 8, and 9. The first event has only partial coverage from RHESSI, due to spacecraft night. Fourth row: examples of AIA EUV emissions from the jet base/top. The blue lines show light curves of a 3" × 3" box at the base of each jet in the 304 Å channel, and the red lines show light curves of a 3" × 3" box at the top of each jet in the 131 Å channel (the boxes are not shown). Bottom row: XRT measurements of the selected regions (3" × 3"; not shown) at the jet base (blue) and the jet top (red), in the thin-Be filter. Both events only have partial coverage from XRT.

for the later jet. Figure 4 shows RHESSI images in 3–12 keV using detectors 3, 6, 8, and 9. All images were produced using the CLEAN algorithm in the HESSI IDL software package. In both events, the HXR emissions were observed near the top of the jet. Furthermore, the time slices of the later jet show that there were actually three HXR sources in that event. The first HXR source appeared at the base of the jet a few minutes after the jet's starting time, and it peaked at around 20:46 UT. The location of this source is consistent with the erupting minifilament site where magnetic reconnection took place. Meanwhile, starting from  $\sim$ 20:46 UT, the second HXR source appeared near the top of the jet, and it became dominant in the period from 20:48 to 20:51 UT. Finally, after the source at the jet top had faded away, another HXR source was observed to the north of the jet, which reached its maximum intensity at  $\sim$ 20:53 UT.

### 2.3. XRT Data

XRT provides additional coverage of high-temperature plasma beyond the AIA hot channels and RHESSI, though only the data in the thin-Be filter are available, for parts of each jet. This filter is sensitive to plasma temperatures around 10 MK, and it shows very similar jet behavior to the AIA 94 Å and 131 Å filters. Here, we include these data as supplementary observations.

The thin-Be filter data are available for the first 15 minutes of the earlier jet (before 17:30 UT), with a cadence of half a minute. The jet started with a very fast flow at  $\sim$ 17:15 UT, and reached its maximum extent in just a few minutes. Then, after  $\sim$ 17:20 UT, it grew slightly wider and remained visible toward the end of the observation time (Figure 5). As for the later jet, XRT missed most of its erupting process, since no data were available between 20:45 UT and 21:09 UT. But after 21:09 UT, the jet was still visible in the thin-Be filter, until it finally faded away at  $\sim$ 22:00 UT (not shown). Similar to the AIA observations, for both events, the brightenings at the jet base (indicated by the white arrows in Figure 5) show the locations of the reconnection sites there.

#### 2.4. IRIS Data

IRIS has full temporal coverage and partial spatial coverage of the earlier jet in its 1330 Å slit-jaw images. This channel is sensitive to temperatures around 0.02 MK, with a spatial resolution of 0."33 and a cadence of 10 s, thus it helps to investigate the dynamics of plasma at chromospheric temperatures. For the earlier event, the jet was at the corner of the field of view, and most of the jet body (but not the jet base or top) was captured in these images (Figure 5). The jet evolution in this channel was similar to that in the AIA 304 Å channel, and we used these data (in addition to the AIA data) to estimate the jet velocities (see Section 3.2). However, this channel had

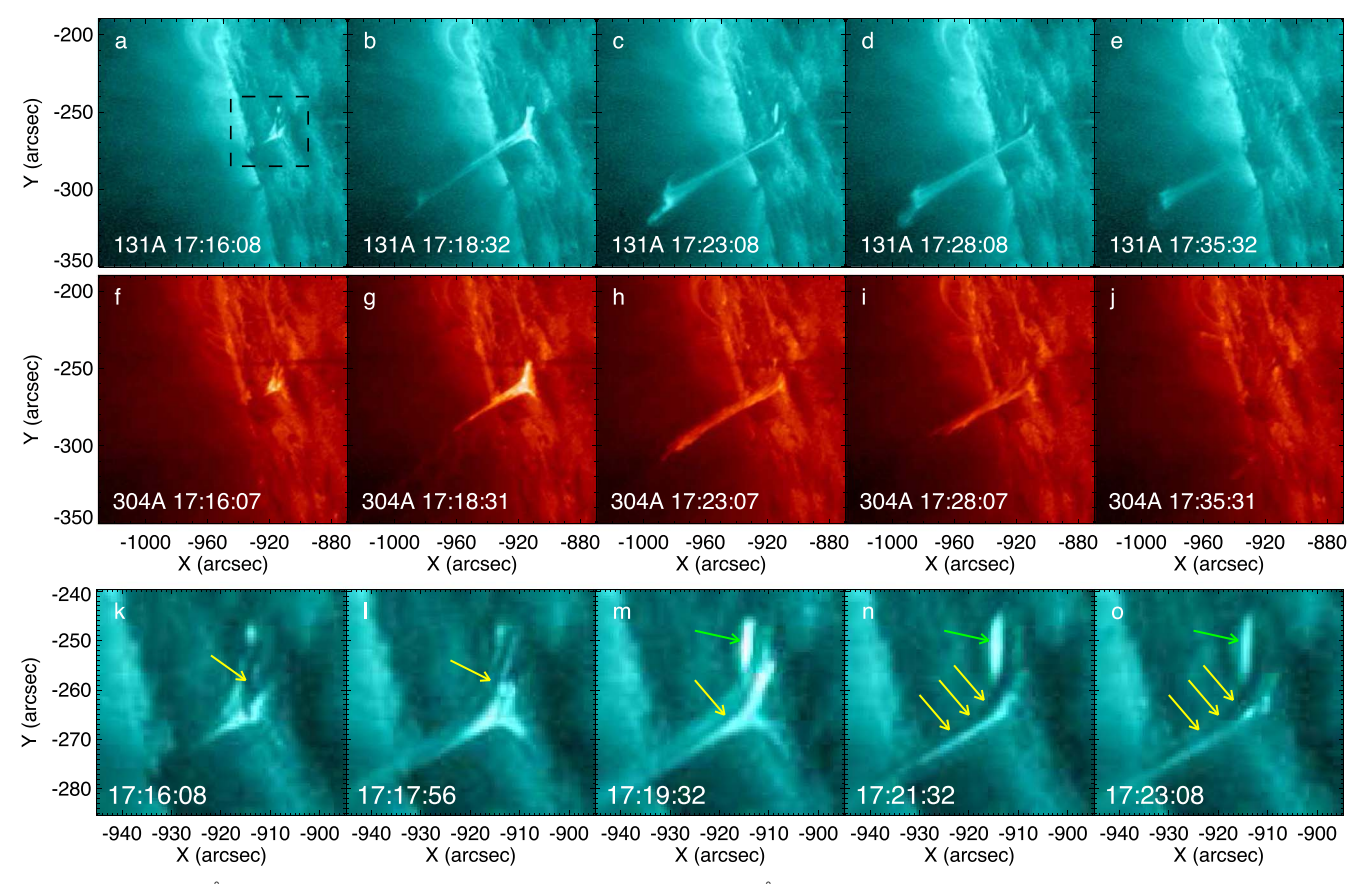


Figure 2. (a)–(e) AIA 131 Å images of the first (17:20) jet at selected times. (f)–(j) AIA 304 Å images of this jet. The jet reached its maximum extent at an earlier time, and lasted longer in the hotter 131 Å channel (sensitive to both  $\sim$ 0.4 MK and  $\sim$ 10 MK temperatures) compared to the cool 304 Å channel (sensitive to chromospheric temperatures around 0.05 MK). (k)–(o) Zoomed-in views—of the region marked by the black dashed box in (a)—of the minifilament eruption at the jet base in the 131 Å channel. The yellow arrows point to the minifilament material, and the green arrows point to the JBP resulting from this eruption. (An animation of this jet is available, which shows the jet's evolution in seven AIA channels from 17:10 UT to 17:39 UT, with a 36 s cadence. The duration of the animation is 5 s.) (An animation of this figure is available.)

much less coverage of the later jet, and it was not considered for that event.

### 3. Data Analysis

#### 3.1. DEM Analysis

We carried out a differential emission measure (DEM) analysis to investigate the temperature profiles for these two events. A DEM describes a plasma distribution with respect to the temperature along the line of sight, and it is directly related to the observed flux F for a particular instrument via

$$F = \int R(T) \cdot \text{DEM}(T) \, dT, \tag{1}$$

where *R* is the temperature response of that instrument. In this analysis, we used the regularization method developed by Hannah & Kontar (2012, 2013) for DEM inversion. We considered two different data selections: (a) the AIA bandpass filter data only, where we used the data from six AIA bandpass filters that are sensitive to coronal temperatures—94 Å, 131 Å, 171 Å, 193 Å, 211 Å, and 335 Å; and (b) a combination of multi-instrument data, where we used the same set of AIA data, together with HXR measurements in the 4–5, 5–6, and 6–7 keV bands from RHESSI, as well as the thin-Be filter data from XRT, if those were available. The RHESSI 4–5 and 5–6 keV

energy bands were selected because they measure plasma temperature via the bremsstrahlung continuum, and the 6–7 keV energy band was particularly important as it includes the 6.7 keV Fe line complex. The uncertainties for the AIA data were estimated via the SSWIDL procedure "aia\_bp\_estimate\_error.pro," which was added in quadrature with a systematic error of 10%. The uncertainties for the RHESSI and XRT data were both estimated as 20%.

The temperature responses for the AIA and XRT filters were generated through the SSWIDL routines "aia\_get\_response.pro" and "make\_xrt\_temp\_resp.pro," respectively. To obtain the temperature responses for RHESSI in different energy bands, we first calculated the isothermal HXR spectra as a function of energy for multiple temperatures, ranging from 3 to 30 MK, using the SSWIDL routine "f\_vth.pro." Thus, for each energy band, we obtained a series of photon fluxes at different temperatures, which would correspond to the temperature response (in photon space) for that energy band, after applying proper normalization. (The RHESSI instrument response had already been taken into account when producing the HXR images, thus it did not need to be included in the temperature response.) In the above calculation, coronal abundances were adopted.

We calculated the DEMs for four regions where HXR emissions were observed, around the times when each HXR source reached its maximum intensity: the top of the earlier jet

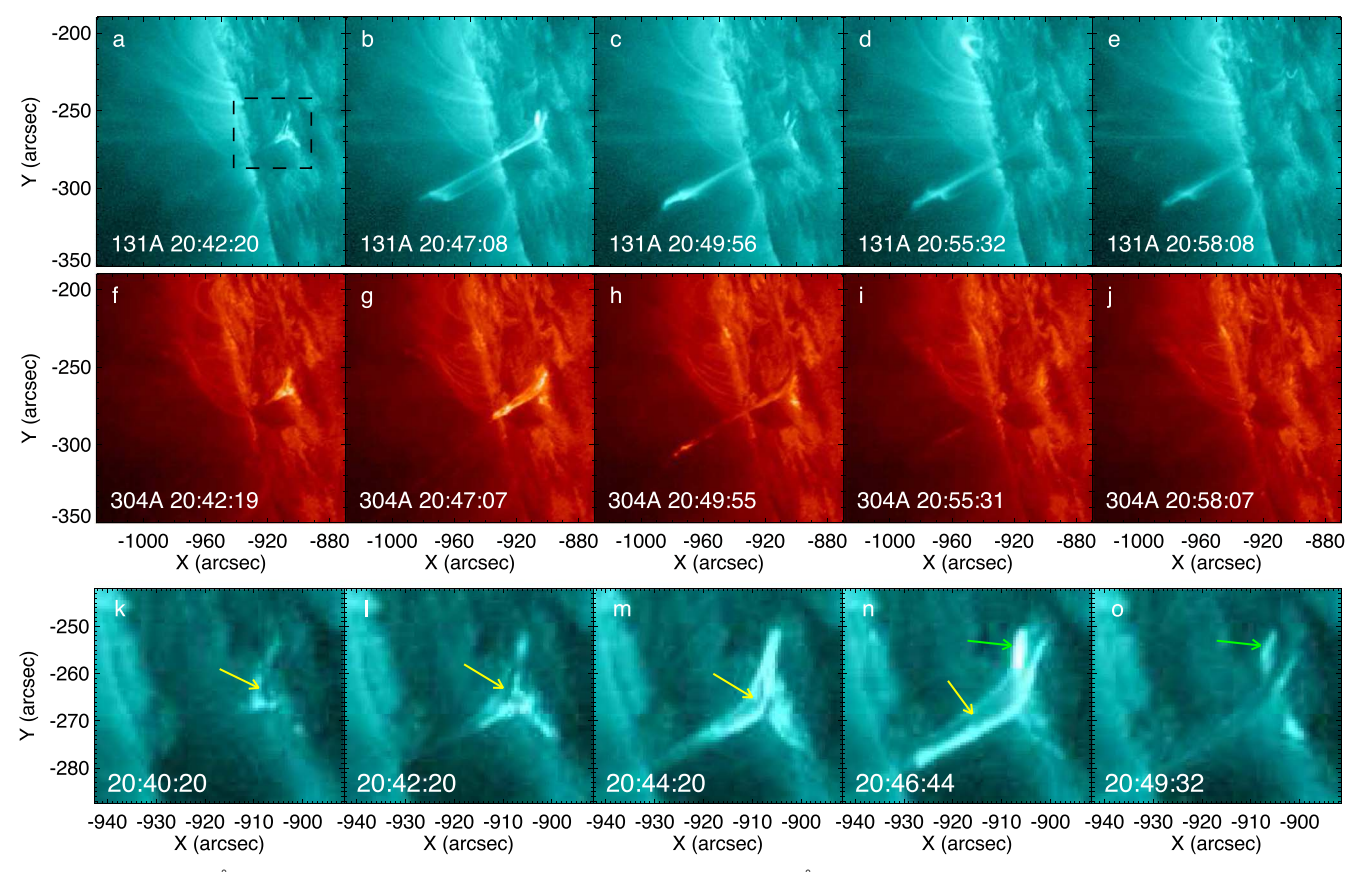


Figure 3. (a)—(e) AIA 131 Å images of the later (20:47) jet at selected times. (f)—(j) AIA 304 Å images of this jet. Similar to the earlier event, the jet reached its maximum extent at an earlier time and lasted longer in the hotter 131 Å channel. (k)—(o) Zoomed-in views—of the region marked by the black dashed box in (a)—of the minifilament eruption at the jet base in the 131 Å channel. The yellow arrows point to the minifilament material, and the green arrows point to the JBP resulting from this eruption. (An animation of this jet is available, which shows the jet's evolution in seven AIA channels from 20:40 UT to 21:19 UT, with a 36 s cadence. The duration of the animation is 6 s.)

(An animation of this figure is available.)

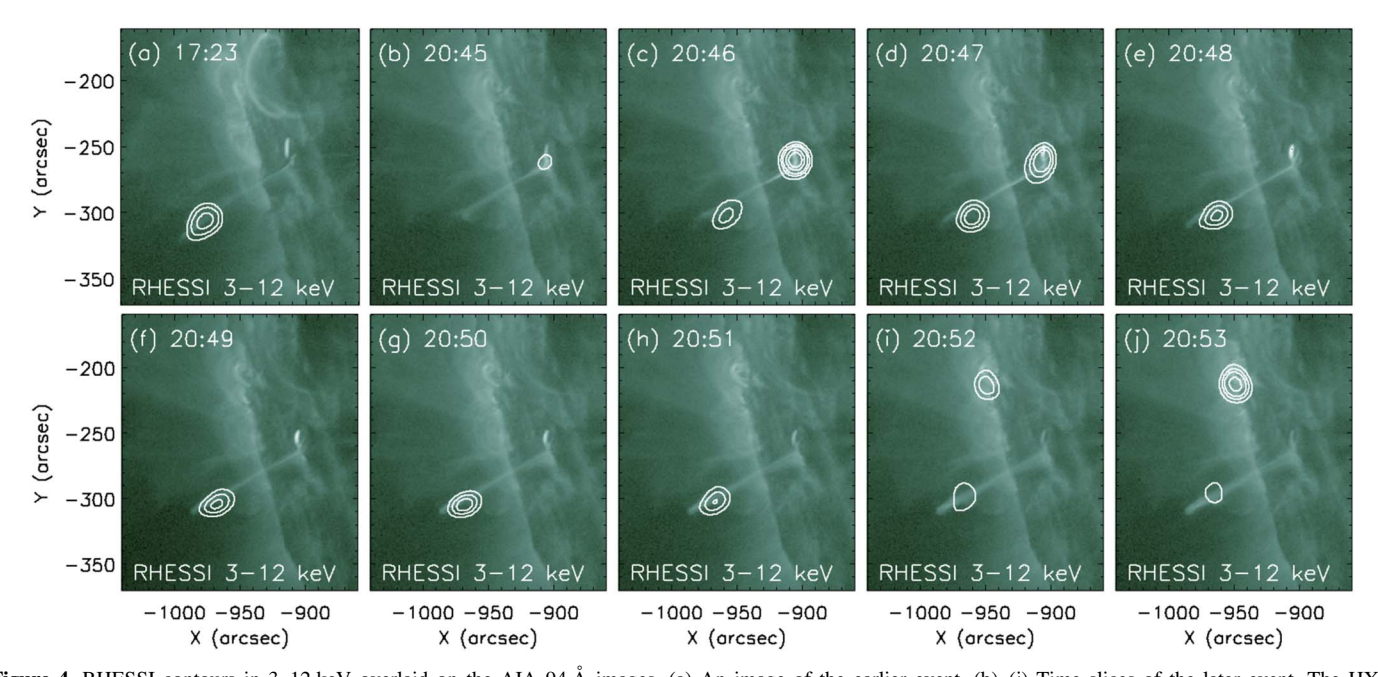


Figure 4. RHESSI contours in 3–12 keV overlaid on the AIA 94 Å images. (a) An image of the earlier event. (b)–(j) Time slices of the later event. The HXR emissions were observed near the top of the jet in both events. The later event showed three different HXR sources: one at the base of the jet at  $\sim$ 20:46 UT (c), one near the top of the jet at  $\sim$ 20:50 UT (g), and one to the north of the jet at  $\sim$ 20:53 UT (j).

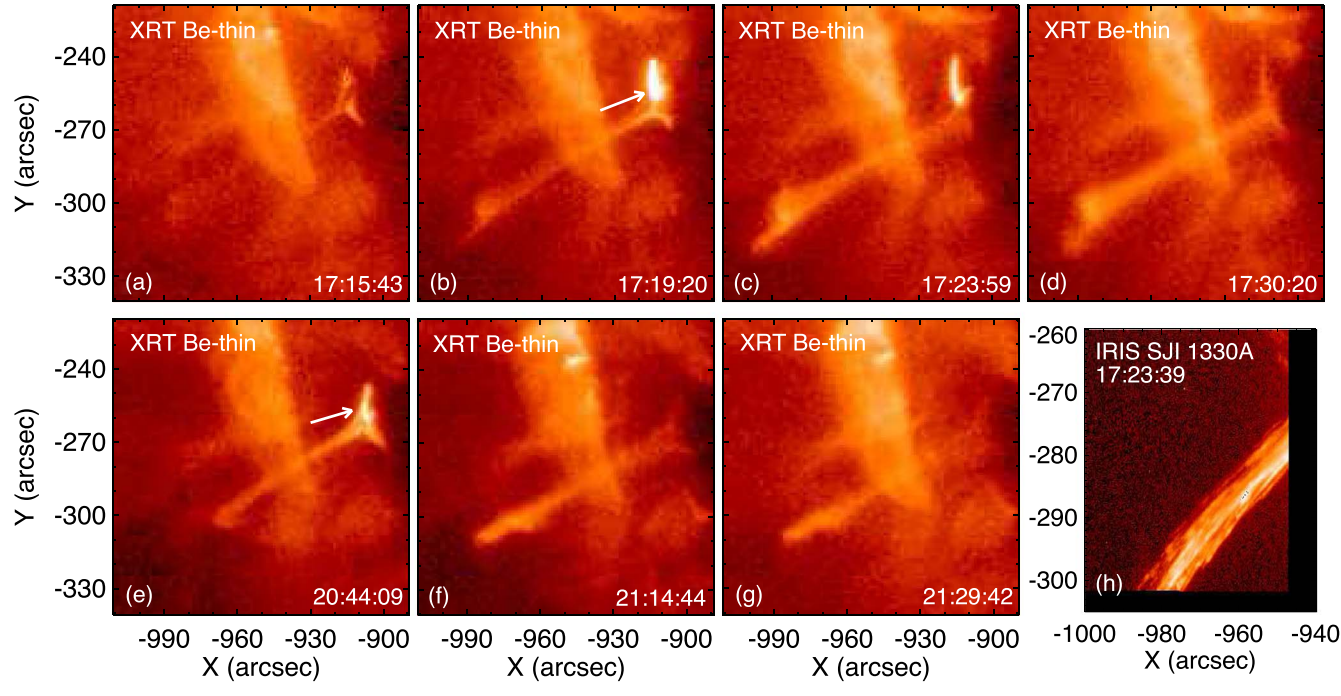


Figure 5. XRT and IRIS images of the two jets at selected times. (a)–(d) XRT thin-Be images of the earlier event. The jet evolution is similar to that in the AIA hot filters (94 Å and 131 Å). (e)–(g) XRT thin-Be images of the later event. No data were available between 20:44 and 21:09 UT. The jet base brightenings, indicated by the white arrows, show the locations of the primary reconnection sites. (h) An IRIS SJI 1330 Å image of the earlier event. The jet was located at the corner of the IRIS field of view.

at 17:24 UT, the base of the later jet at 20:46 UT, the top of the later jet at 20:50 UT, and the loop to the north of the later jet at 20:53 UT. Each region was selected based on contours in the AIA 131 Å images, and the observed intensities were averaged over the whole region. We first obtained the DEM results using AIA data only (the black lines in Figure 6), as well as the corresponding residuals in data space (the asterisks in Figure 6). All these AIA-only DEMs indicate the existence of multithermal plasma, each with a high-temperature component peaking around 10 MK. However, although these AIAonly DEMs had good enough predictions in the AIA channels that were used for the DEM inversion, they failed to predict the HXR measurements well. As shown by the blue asterisks in the residual plots, the photon fluxes predicted by the AIA-only DEMs in the RHESSI 4-5 and 5-6 keV energy bins were always lower than the actual measurements, and the line emissions in the 6-7 keV energy bin were very prominent compared to the bremsstrahlung continuum.

To gain a better understanding of the level of agreement between AIA and RHESSI, we carried out a more complete quantitative comparison of the HXR fluxes between the two instruments. In this exercise, we predicted the HXR spectrum in the 3–15 keV energy range for the top region of the earlier jet using the AIA-only DEM, and compared it with the spectrum directly measured by RHESSI. The predicted HXR spectrum was calculated according to Equation (1), with R being the RHESSI temperature response. The results are shown in the left panel of Figure 7, where the AIA-predicted HXR fluxes were consistently lower than the RHESSI fluxes, indicating a possible cross-calibration factor between AIA and RHESSI. Again, the AIA-only DEM predicted much stronger line emissions in the 6-7 keV energy bin over the continuum, as compared to the actual RHESSI observations. The reasons for these disagreements could have to do with some instrumental

effects that are not well understood, such as the change in RHESSI blanketing with respect to time, or could involve possible "nonstandard" elemental abundances in these events that we are unable to characterize.

Because of the discrepancies mentioned above, incorporating RHESSI data into this DEM analysis is challenging. To obtain a DEM solution that could successfully predict both the HXR continuum and the line feature at the same time, we found that a cross-calibration factor between AIA and RHESSI was required, plus the initial DEM guess must also be very carefully chosen. We had the best chance of success when using a "modified" AIA-only DEM as the initial guess, where we substituted the high-temperature component of each AIAonly DEM with a Gaussian distribution that peaked around the temperature given by the RHESSI spectroscopy (more details of the spectroscopy will be discussed in Section 3.3). The height, width, and exact peak location of that Gaussian distribution were tested with a series of values, and we selected the most robust ones. In this piece of analysis, we scaled down the photon fluxes from RHESSI by a factor of 3.5, but this cross-calibration factor could be in the range of 3-5 and was not well constrained. Incidentally, this factor that we found here is similar to the AIA-RHESSI discrepancy that was found by Battaglia & Kontar (2013). In addition, in some literature, a factor of 2-3 has been suggested for cross-calibration between AIA and XRT (e.g., Schmelz et al. 2015; Wright et al. 2017). We found that multiplying a factor of 2 to the XRT response would result in a better agreement between the predicted and measured thin-Be filter data; thus, that factor was also included here.

The joint DEMs (red lines) and the data-space residuals (red triangles) are also plotted in Figure 6, along with the AIA-only DEM results. These joint DEMs are the only set of solutions we found that fit both the line emission and the bremsstrahlung

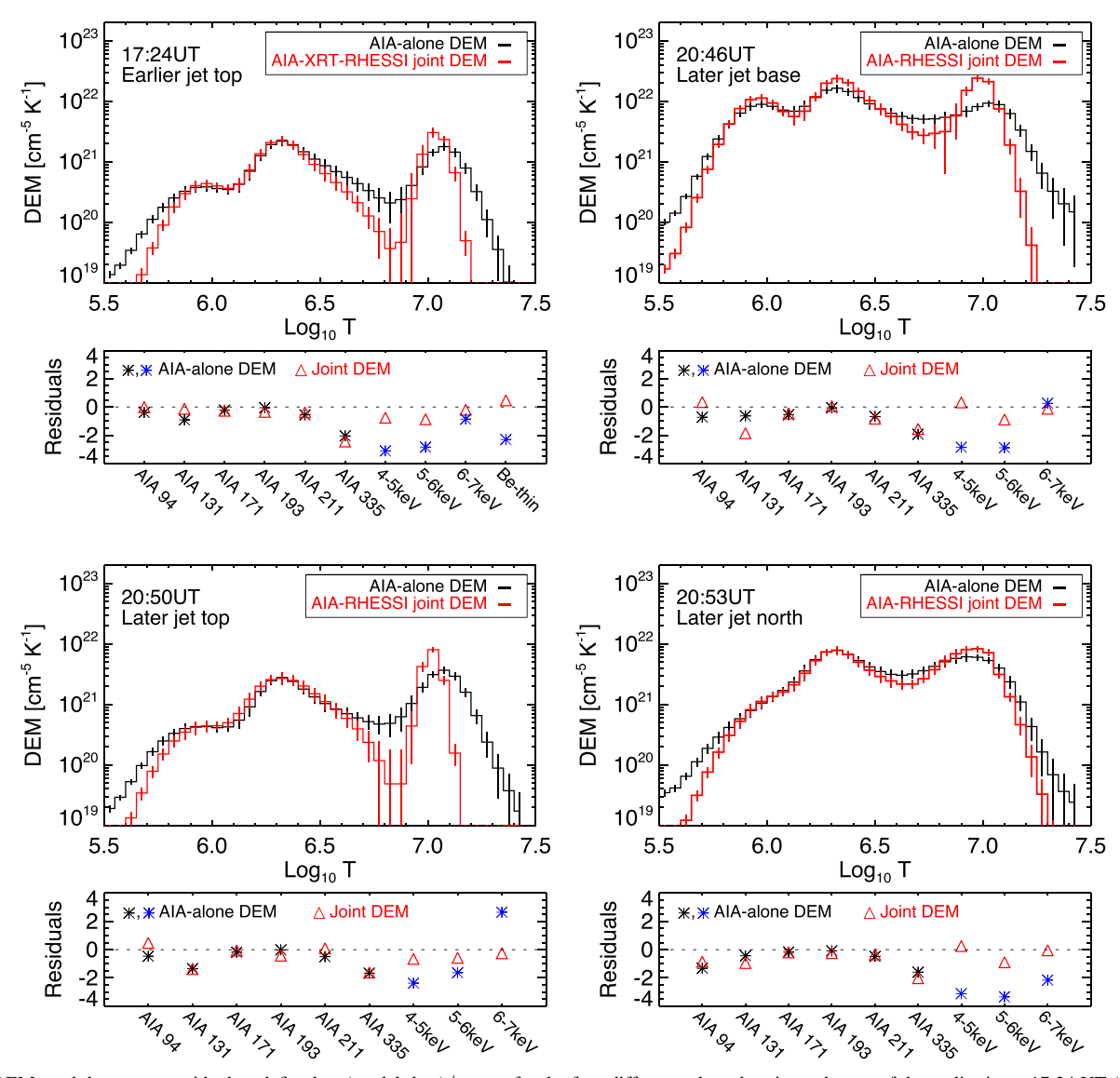
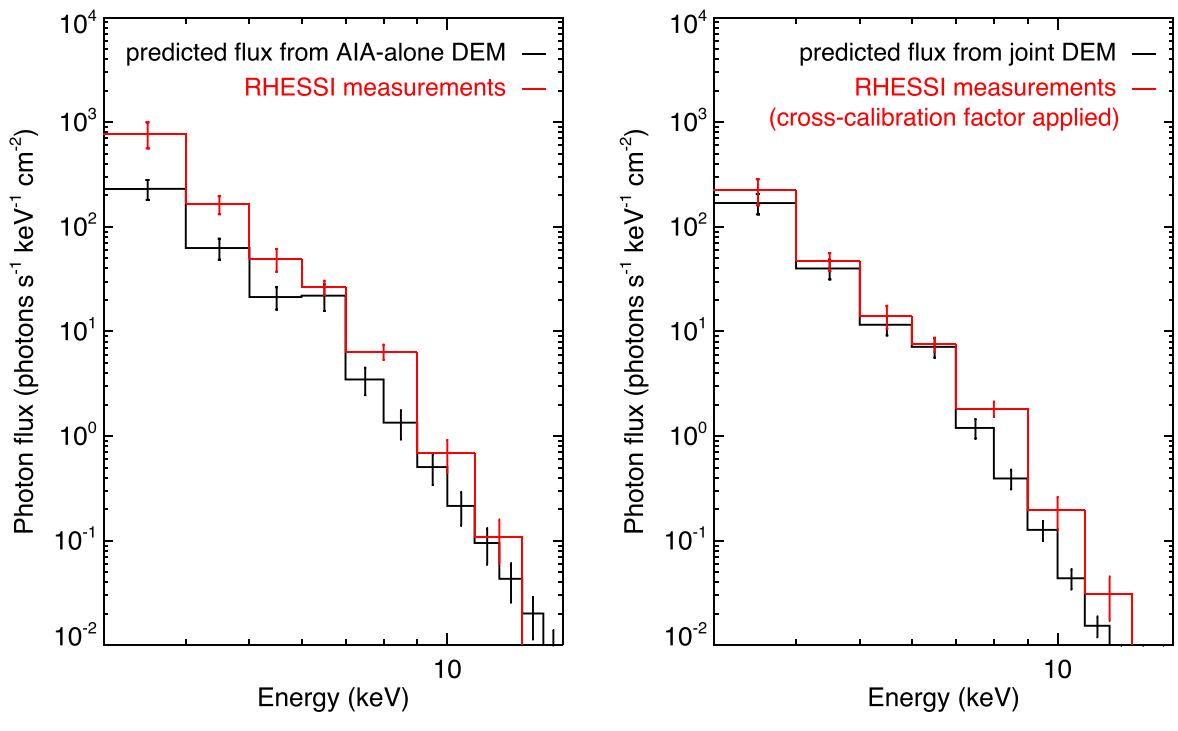


Figure 6. DEMs and data-space residuals—defined as (model-data)/error—for the four different selected regions: the top of the earlier jet at 17:24 UT (top left), the base of the later jet at 20:47 UT (top right), the top of the later jet at 20:49 UT (bottom left), and a loop to the north of the later jet at 20:53 UT (bottom right). The black lines show the results for the DEM inversions that used AIA data only, and the red lines show the results for the DEM inversions that used multi-instrument data from AIA, RHESSI, and XRT, if available. The AIA-only DEMs and the joint DEMs agree qualitatively, but the joint DEMs require a more isothermal and slightly cooler high-temperature component for each source. In the residual plots, the asterisks show the results from the AIA-only DEMs (with the black asterisks showing the residuals in the AIA channels that were used for the DEM inversions, and the blue asterisks showing the residuals in the RHESSI energy bands and possibly the XRT thin-Be filter predicted by this DEM), while the red triangles show the results from the joint DEMs. The HXR fluxes predicted by the joint DEMs have much better agreement with the actual data.

continuum well. For all the selected regions, the joint DEMs have very similar cool components to the AIA-only DEMs, but the hot components of the joint DEMs tend to be more isothermal and slightly cooler. In particular, the HXR constraints significantly reduced the amount of plasma above  $\sim\!15$  MK (otherwise the predicted line emission was always too prominent). However, previous studies have seen larger discrepancies between bandpass filter DEMs and the ones that included HXR constraints. For example, in the DEM analysis for a quiescent active region presented by Schmelz et al. (2009), a high-temperature component that peaked around  $10^{7.4}$  K was found when using data only from the XRT filters, but the DEM for that component was reduced by more than one order of magnitude when combining the observations from both XRT and RHESSI. Compared to that study, the AIA-only DEMs

here are not too far from the joint DEMs that incorporated HXR data.

We further compared the HXR fluxes predicted by the joint DEM with the RHESSI measurements (with a cross-calibration factor applied) for the top region of the earlier jet, as shown in the right panel of Figure 7. As expected, the two HXR spectra had much better agreements at lower energies than did the spectra predicted from the AIA-only DEMs, including both the overall continuum and the line feature. Besides, for higher energies around 10 keV, the RHESSI measurements had systematically higher emissions, suggesting a possible non-thermal component for this source. This is consistent with our later findings through spectral analysis (Section 3.3). As a side note, later spectral analysis suggests that for some of the HXR sources, nonthermal emissions might dominate in the 6–7 keV



**Figure 7.** Left: HXR spectrum for the source at the top of the earlier jet, deduced from the AIA-only DEM (black), compared to the RHESSI measurements (red). Right: HXR spectrum for the same source, deduced from the joint DEM (black), compared to the RHESSI measurements with a cross-calibration factor applied (red). With a cross-calibration factor of 3.5, the HXR spectrum from the joint DEM could successfully predict the bremsstrahlung continuum and the line feature at 6.7 keV simultaneously.

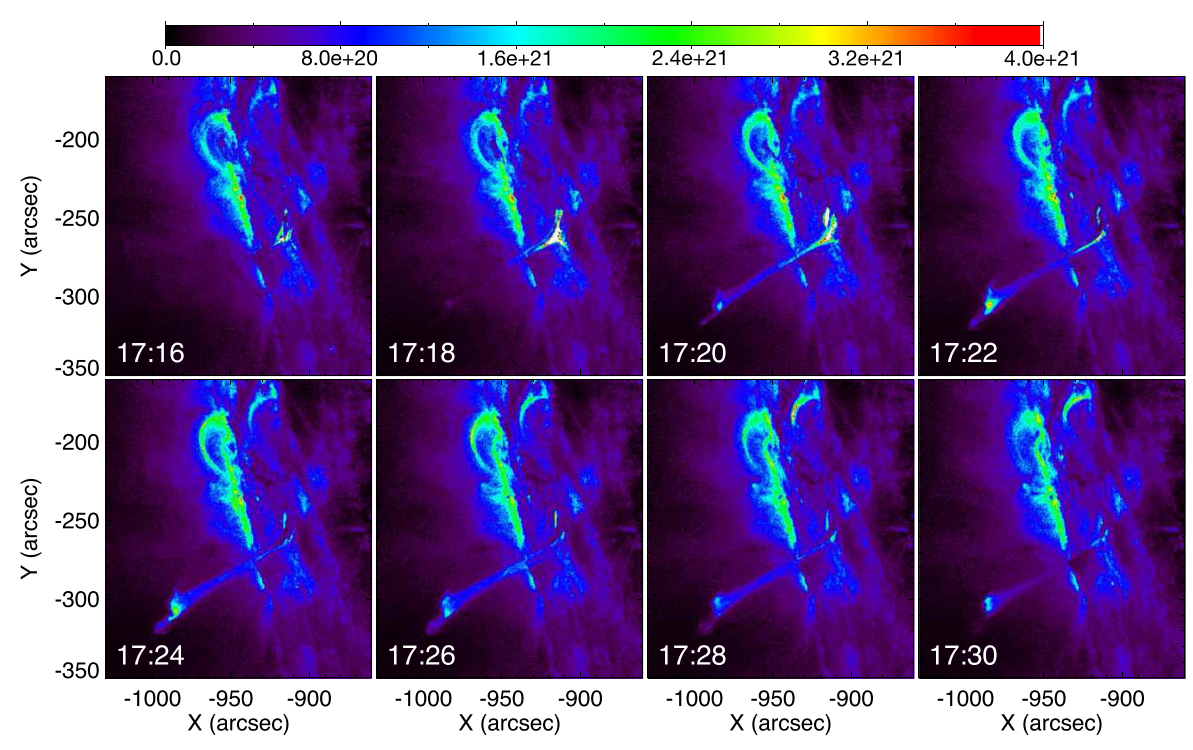


Figure 8. Temporal evolution of the DEM maps in 11–14 MK for the earlier jet. Hot plasma appeared at the base of the jet during the first few minutes, but starting from  $\sim$ 17:20, more and more hot plasma was observed near the top of the jet, and the top source became dominant at  $\sim$ 17:22. The color scale is in units of cm<sup>-5</sup> K<sup>-1</sup>.

(and maybe 5–6 keV) energy bin(s). In this scenario, the fluxes from those thermal sources would be even lower, and the joint DEMs shown here provide upper limits for the possible amount of hot plasma.

As the final part of the DEM analysis, we examined the temporal evolutions of the DEM maps in 11–14 MK (i.e., the hot component) for each event (Figures 8 and 9). Because of the missing RHESSI and XRT data, and the fact that the AIA-

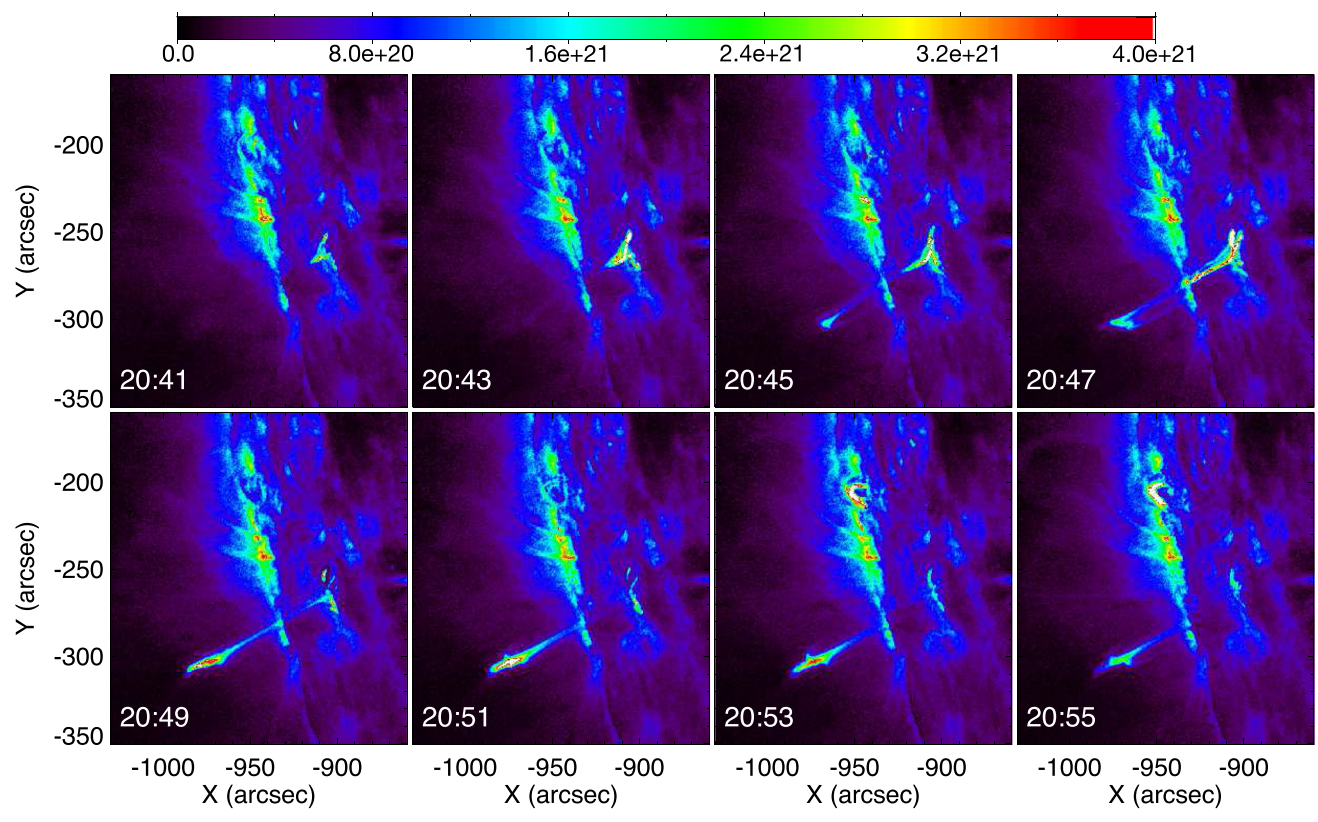


Figure 9. Temporal evolution of the DEM maps in 11–14 MK for the later jet. Similar to the earlier event, hot plasma first appeared at the base of the jet, but was also observed near the top of the jet, starting from  $\sim$ 20:45, with the top source becoming dominant at  $\sim$ 20:50. The color scale is in units of cm<sup>-5</sup> K<sup>-1</sup>.

only DEMs in this temperature range qualitatively agree with the joint DEMs, these DEM maps were all generated using AIA data only. In both events, hot plasma first appeared at the base of the jet (the same location from where the minifilament erupted and magnetic reconnection occurred); however, as the hot plasma at the jet base gradually cooled down, more and more hot plasma was observed near the top of the jet, and that location was mostly stationary. These DEM maps show consistent results with the location and temporal evolution of the RHESSI HXR sources.

### 3.2. Jet Velocities

Identifying the different velocities associated with the jet could be helpful for differentiating the possible mechanisms behind those jets. A common method for velocity estimation is making time–distance plots (e.g., Mulay et al. 2016; Musset et al. 2020). Such plots are usually produced by putting together time slices of the intensity profile along the direction of the jet, in which case the jet velocities (in the plane of the sky) are the slopes. To take into account everything within the width of the jets, we here selected a rectangular region around each jet, and we summed the intensities across the width of this region.

Figure 10 shows the time–distance plots for the earlier jet, using seven EUV filters of AIA and the slit-jaw 1330 Å filter of IRIS. Interestingly, the chromospheric filters (AIA 304 Å and IRIS 1330 Å) are the ones where the velocities are most clearly identified, and they show very consistent results. The 304 Å filter shows multiple upward velocities, ranging from 104 to 226 km s<sup>-1</sup>, while the 1330 Å filter shows upward velocities ranging from 83 km s<sup>-1</sup> to 404 km s<sup>-1</sup> (the uncertainties for

those velocities are on the order of 10%–20%, considering the pixel size and the temporal cadence of the images). Also, both filters clearly indicate that some plasma returned to the solar surface (likely) along the same trajectory as the original jet, with downflow velocities of 110– $140~{\rm km~s^{-1}}$ . For the rest of the AIA filters, similar upward and downward velocities to those mentioned above can be partially seen in the  $171~{\rm \AA}$  filter (sensitive to  $\sim$ 0.6 MK plasma), but could barely be seen in other ones. However, there were also some really fast outflows at the beginning of this jet in the  $131~{\rm \AA}$  filter (sensitive to both  $\sim$ 0.4 and  $\sim$ 10 MK plasma), which has a velocity of  $\sim$ 700 km s<sup>-1</sup>.

The time–distance plots for the later jet present a slightly different picture (Figure 11). The 304 Å filter again shows multiple upward velocities, ranging from 192 km s<sup>-1</sup> to 251 km s<sup>-1</sup>, and downward velocities around 130 km s<sup>-1</sup> (the uncertainty is on the order of 10%–20%). However, these main upward velocities can be clearly identified in all seven AIA filters, including both cool and hot ones. Additionally, in the 131 Å filter, a faster outflow at the beginning of the jet is still identifiable, but much weaker compared to the earlier event, and the velocity for this outflow is 377 km s<sup>-1</sup>. These velocities will be compared to other studies and to models in Section 4.1.

### 3.3. Imaging Spectroscopy

To study the accelerated electron populations in these events, we performed imaging spectroscopy for the four HXR sources observed by RHESSI. For each source, a 1 minute time interval, during which the source reached its maximum HXR intensity, was first selected by eye, based on the RHESSI images. These images were produced using the CLEAN

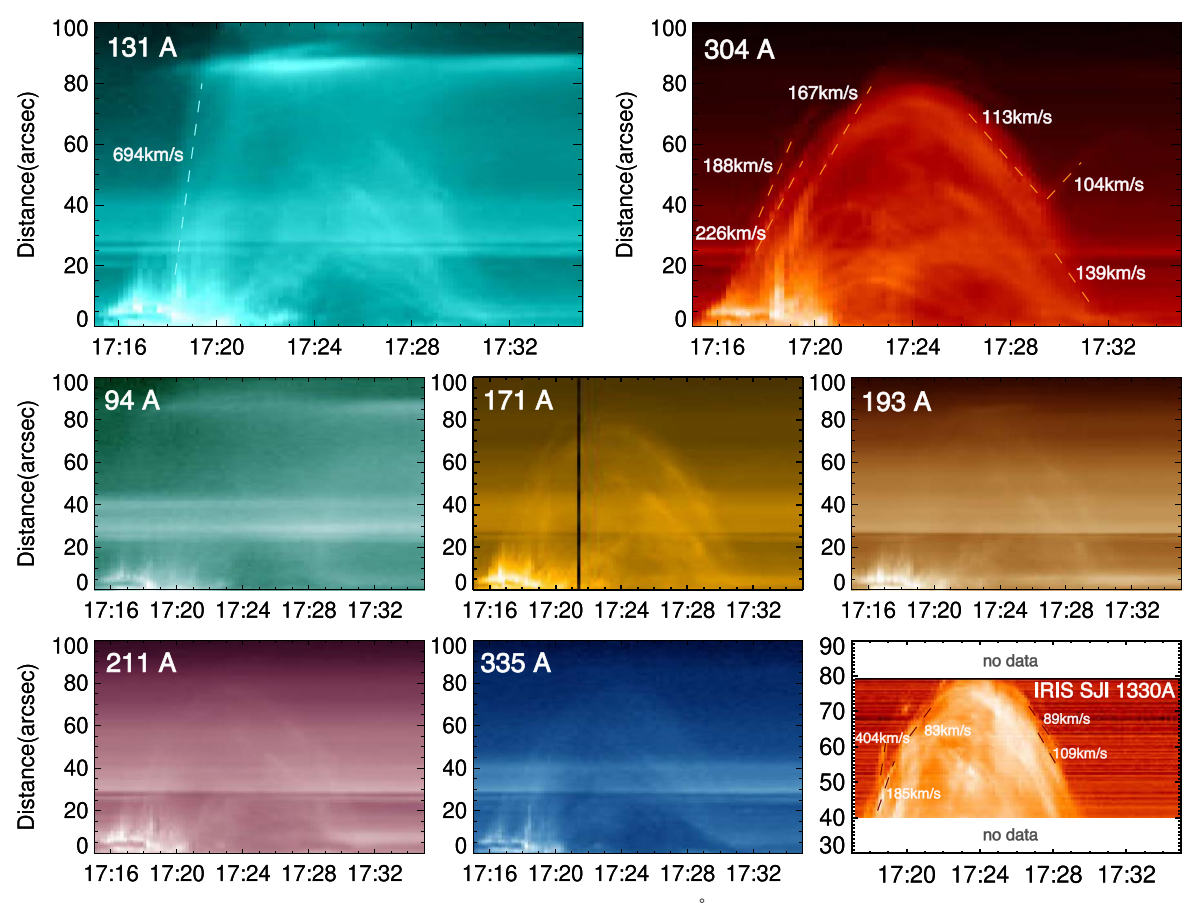


Figure 10. Time-distance plots of the earlier jet in seven AIA EUV filters and the IRIS 1330 Å filter. The slopes for the velocity calculation are shown as the dashed lines. The chromospheric filters (AIA 304 Å and IRIS 1330 Å) show various upward velocities around 200 km s<sup>-1</sup> and downward velocities around 110 km s<sup>-1</sup>. The AIA 131 Å filter (sensitive to both  $\sim$ 0.4 and  $\sim$ 10 MK) shows a faster upward velocity of 694 km s<sup>-1</sup> at the beginning of the jet. In the rest of the AIA filters, the velocities are less apparent. (The black line at  $\sim$ 17:21 in the 171 Å plot is due to some instrument issue.)

algorithm and detectors 3, 6, 8, and 9. We then chose a circular region containing that source and obtained the spectrum for the selected region. Finally, we carried out spectral fitting, using the OSPEX software package, in the energy range of 3–15 keV.

As mentioned in Section 3.1, the comparison of the joint DEM and RHESSI measurements suggests a nonthermal component in the HXR spectrum. To further confirm this, we first fitted the spectra with an isothermal model (not shown), but the models always overpredicted the fluxes at the 6.7 keV line complex, and had systematically low emissions at energies above 10 keV for all the sources. This indicated that there should be another component in the spectra, either due to a second thermal distribution or a nonthermal distribution. However, the results of the fitting for a double thermal model (not shown) had unphysical fit parameters for one of the thermal components, and it again overpredicted the line emission, making this scenario unlikely. Therefore, we confirmed that there should be nonthermal emissions in these events. We then added a thick-target nonthermal component to the fitting (the justification for the thick-target regime will be discussed in Section 4.2), and we could obtain good fits across the entire observed energy range. (We used the temperatures from those fits as a reference when generating the initial DEM guess for the joint DEM inversion.) However, due to the limited number of energy bins and the number of free parameters, some of the fit parameters were not well constrained and had uncertainties over 100%. To further reduce the uncertainties, we performed another fitting, with a

fixed temperature, which was chosen to be the average temperature of the hot component derived from the joint DEMs. The resulting spectra are shown in Figure 12, and the parameters are reported in Table 1. Interestingly, the non-thermal electron power laws in all sources have similar spectral indices around 10 and low-energy cutoffs around 9 keV. While these nonthermal power laws are steeper than in most flares, the parameters are consistent with the range found for microflares by Hannah et al. (2008).

### 4. Discussion

## 4.1. Jet Velocities and Driving Mechanisms

In these two events, we observed two types of upward velocities in the jets. One type falls within the range of 80–400 km s $^{-1}$ , most clearly seen in the AIA 304 Å and IRIS 1330 Å filters (sensitive to chromospheric temperatures), and possibly visible in other filters. This type of velocity is consistent with many previous studies of coronal jets (e.g., Shimojo et al. 1996; Savcheva et al. 2007; Mulay et al. 2016; Panesar et al. 2016a; Musset et al. 2020), where the jet velocities usually range from a few tens of km s $^{-1}$  to  $\sim\!500$  km s $^{-1}$ , with an average around 200 km s $^{-1}$ . The other velocities,  $\sim\!700$  km s $^{-1}$  and  $\sim\!400$  km s $^{-1}$ , respectively, for the two jets, could only be identified in the 131 Å filter (sensitive to  $\sim\!0.4$  MK and hot temperatures  $\sim\!10$  MK) at the beginning of each event (though harder for the later jet). The velocity of  $\sim\!400$  km s $^{-1}$  is still within the common range for coronal jets, but it is faster than the other

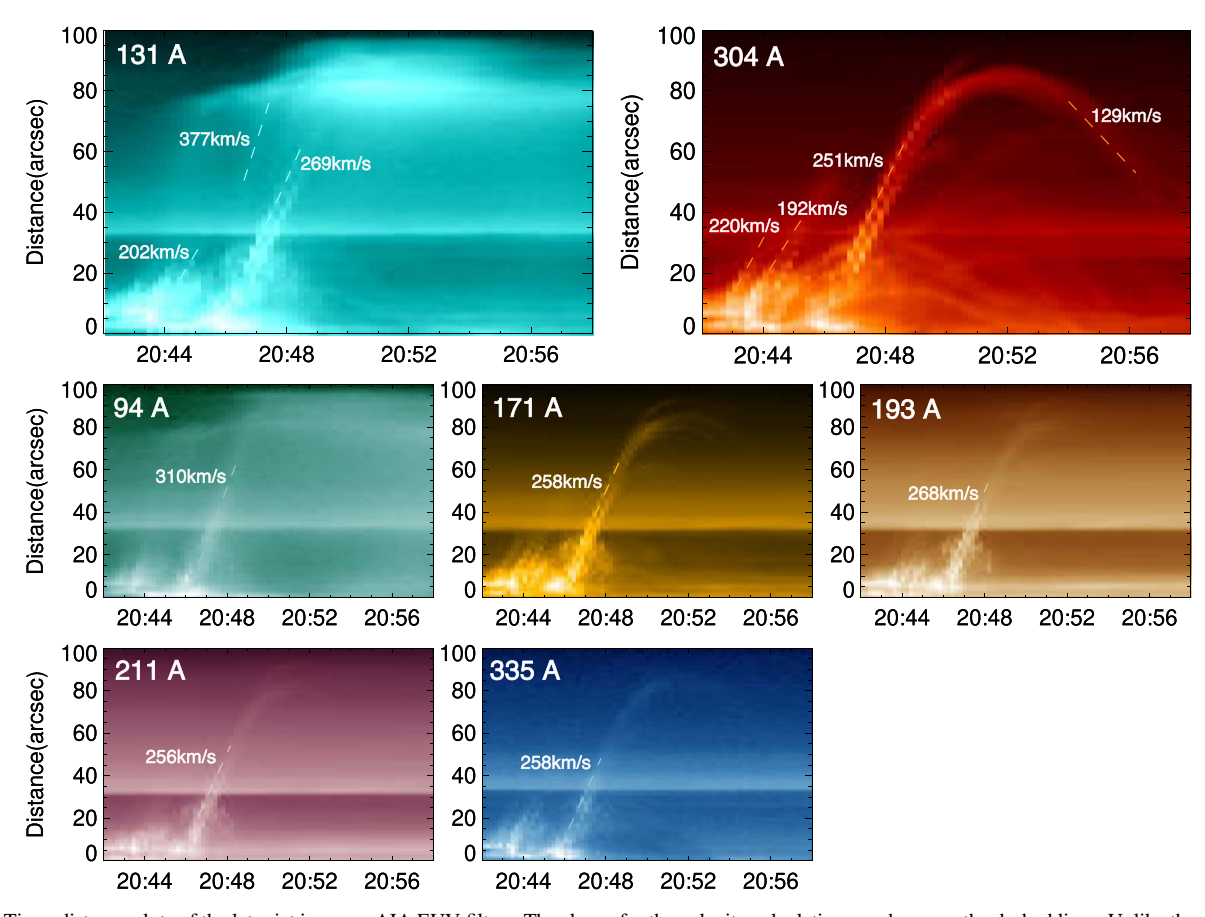


**Figure 11.** Time–distance plots of the later jet in seven AIA EUV filters. The slopes for the velocity calculation are shown as the dashed lines. Unlike the earlier event, the main upward velocities can be clearly identified in all the filters. The AIA 131 Å filter still shows a faster upward velocity of 377 km s<sup>-1</sup> at the beginning of the jet, but this velocity is less apparent.

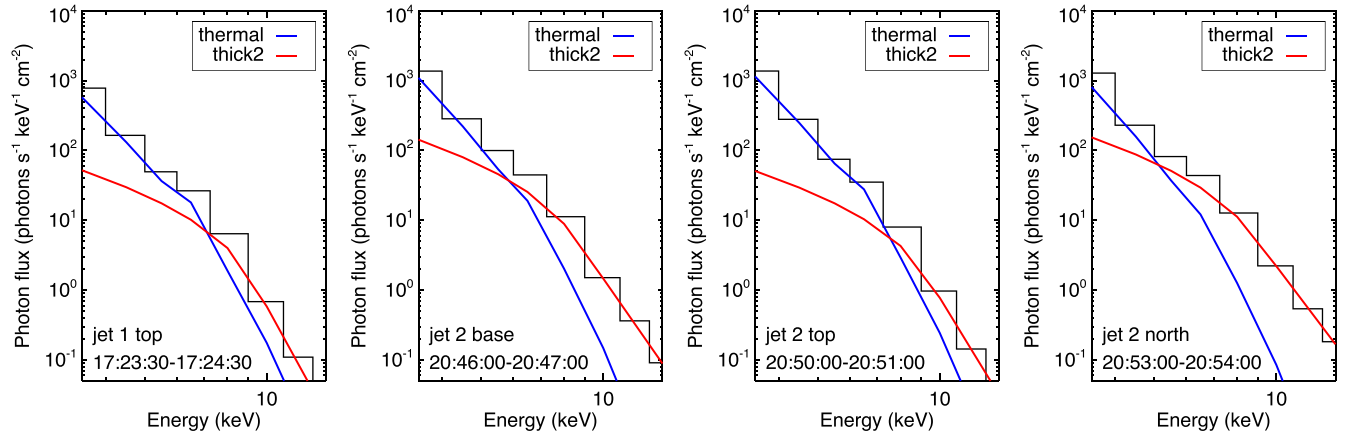


**Figure 12.** RHESSI spectra for the four HXR sources observed in these two events, each during a 1 minute interval when the source approximately reached its maximum HXR intensity. All spectra can be well fitted with an isothermal (blue) plus thick-target (red) model. Note that in these fits, the isothermal temperatures were fixed to be the average temperatures of the hot components derived from the joint DEMs.

Table 1
Fit Parameters for the Four RHESSI HXR Sources, Assuming an Isothermal Plus Thick-target Model

	Time	Emission Measure (10 <sup>46</sup> cm <sup>-3</sup> )	Temperature (MK, fixed)	Spectral Index	Low-energy Cutoff (keV)
Jet 1 top source	17:23:30–17:24:30	$1.8 \pm 0.5$	11.1	$11.4 \pm 3.6$	9.3 ± 1.6
Jet 2 base source	20:46:00-20:47:00	$4.7 \pm 1.0$	9.9	$9.1 \pm 0.9$	$8.5 \pm 0.9$
Jet 2 top source	20:50:00-20:51:00	$4.1 \pm 0.5$	10.5	$10.3 \pm 1.4$	$9.4 \pm 1.2$
Jet 2 northern source	20:53:00-20:54:00	$3.9 \pm 1.3$	9.6	$8.5\pm0.8$	$8.7 \pm 1.0$

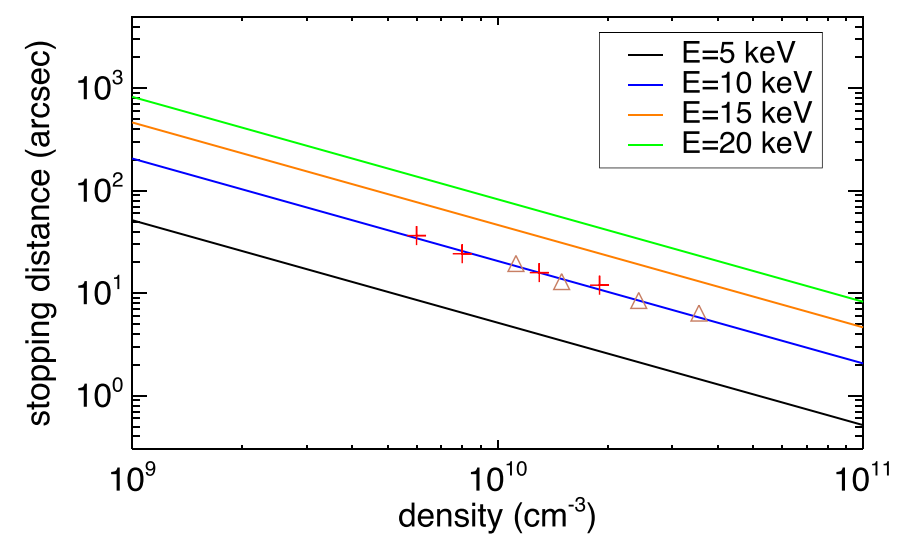


Figure 13. The relation between the collisional stopping distances and ambient plasma densities for electrons of certain energies. The red plus signs mark the values of the densities (without a cross-calibration factor) and the average energies for the four observed HXR sources, while the brown triangles mark the values with a cross-calibration factor applied. The stopping distances for these sources are less than a few tens of arcseconds, but for lower densities and/or higher electron energies, accelerated electrons could travel an appreciable distance in the corona.

velocities observed in that jet. The velocity of  $\sim$ 700 km s<sup>-1</sup> seems to be faster than most of the observed jets. However, such velocities are not rare, and have been reported in a few coronal jet observations by XRT (Cirtain et al. 2007; Savcheva et al. 2007).

One possible acceleration mechanism for coronal jets is chromospheric evaporation, which is also the responsible mechanism for some plasma flows in solar flares. In this process, the energy released from magnetic reconnection is deposited in the chromosphere, where it compresses and heats the plasma there, and produces a pressure-driven evaporation outflow on the order of sound speed. In fact, Fisher et al. (1984) derived a theoretical upper limit for the velocity of this evaporation outflow as 2.35 times the local sound speed, where the sound speed  $c_s$  can be calculated as  $c_s = 147\sqrt{\frac{r}{1\text{MK}}} \text{ km s}^{-1}$ , assuming an isothermal model (e.g., Aschwanden 2005). In the 304 Å filter (characteristic temperature: 10<sup>4.7</sup> K), this upper limit corresponds to a very low speed of 77 km s<sup>-1</sup>, indicating that the cool plasma is unlikely to be driven by chromospheric evaporation. Also, the common velocities reported by observations of chromospheric evaporation usually fall within the range of tens of km s<sup>-1</sup> up to 400 km s<sup>-1</sup> (e.g., Doschek et al. 2013; Sadykov et al. 2015; Tian et al. 2015), thus it seems that chromospheric evaporation is not able to explain the very fast flow of the earlier jet observed in the hot 131 Å filter. Furthermore, it is expected that the velocity would increase with the temperature, if a jet should be generated by chromospheric evaporation (Matsui et al. 2012), but here we have seen very consistent velocities in all seven AIA filters that are sensitive to different temperatures in the later event. For all these reasons, if both jets are driven by the same mechanism, that mechanism is likely not chromospheric evaporation, but magnetic tension instead. However, it is not clear why the earlier jet shows more complicated and various velocities (even in a single channel), if both jets are driven similarly.

We also note that the freefall velocity corresponding to a height of 80'' is  $179~{\rm km\,s}^{-1}$ , which is smaller than some of the upward-erupting velocities and likely larger than the final

returning velocities. This suggests that the plasma did not decelerate or accelerate solely under the influence of gravity.

#### 4.2. Particle Acceleration Locations

In Section 3.3, we fitted the RHESSI spectra of the four HXR sources with an isothermal plus thick-target model. Here, we first justify that the thick-target regime is a reasonable approximation. Note that in the following calculations, we assume a plasma filling factor of 1.

The column depth (defined as  $N_s = \int n dz$ , where n is the plasma density) to fully stop an electron of energy E (in units of keV) can be calculated as:  $N_s = 1.5 \times 10^{17} \text{cm}^{-2} E^2$  (e.g., Krucker et al. 2008). Based on this formula, Figure 13 plots the relation between the stopping distance and the plasma density for a given electron energy. Under the thick-target regime, according to Table 1, the average electron energy for the source at the top of the earlier jet is  $\sim 10$  keV, and the density there is  $6 \times 10^9$  cm<sup>-3</sup> (derived from the joint DEM), which corresponds to a distance of 36" on average that the electrons can travel before they are fully stopped by the ambient plasma. Similar average electron energies around 10 keV are found for the three other HXR sources in the later event, and the densities of those sources are  $(0.8-1.9) \times 10^{10}$ cm<sup>-3</sup>, resulting in stopping distances of 10"–28". Moreover, in Section 3.1, we report a possible cross-calibration factor around 3.5 between AIA and RHESSI. That factor is not included in the above calculation; however, if the cross-calibration factor is included, all the densities above would be multiplied by  $\sqrt{3.5}$ , corresponding to even shorter stopping distances of 5"-20". And if the plasma filling factor is less than 1, then the densities would be higher, thus the stopping distances would be shorter. In general, these stopping distances are comparable to (or even smaller than) the size of the HXR sources, meaning that accelerated electrons deposit a considerable portion of their energies into each source. Furthermore, if this is a thin-target regime, the spectral indices would be slightly smaller, but the average electron energies would still be  $\sim 10$  keV. This would result in very similar stopping distances that are comparable to the source sizes, which is not consistent with the thin-target assumption. Therefore, we conclude that the HXR sources observed in these events can be approximated as thick targets, and that mildly accelerated electrons are found at all these locations.

Since the three HXR sources observed in the later event share similar electron distributions, here comes the next question: were the HXR emissions in the later event produced by the same population of accelerated electrons, which traveled to different locations; or were they produced by different groups of accelerated electrons individually? In the standard jet models, reconnection occurs near the base of the jet, which would require electrons to be accelerated near the base and travel upward along the magnetic field lines to produce the HXR source at the jet top. However, from the DEM analysis, we find that the densities in the body of the jet (where there were not many HXR emissions) are  $\sim 1 \times 10^{10}$  cm<sup>-3</sup>, so the stopping distance along the jet body is still 20"-30" (for both jets). This is a few times smaller than the distance from the jet base to the jet top (80''-90''); therefore, the HXR source at the top of each jet was produced by electrons that were accelerated very close to this source, rather than electrons that traveled far from the primary reconnection site at the jet base. This finding is in line with a similar one made for the powerful X8.3-class flare on 2017 September 10, obtained with an entirely different methodology that employs microwave imaging spectroscopy (Fleishman et al. 2022).

Another possible explanation for the sources at the jet top could be that the jets were actually ejected along large closed loops perpendicular to the plane of the sky, rather than the socalled "open" field lines. We observe a downward hook-like structure at the top of each jet-e.g., Figure 2(c) and Figure 3(b). In this scenario, the top of the jet would in fact be the apex of the loop, which would have higher emissions because of the line-of-sight effect. The other ends of the loops would be hidden behind the solar limb. However, that hooklike structure was only visible in the hot AIA channels (94 A and 131 Å), and in the 304 Å channel, the movie of the first event clearly shows that some plasma returned to the same location from which the jet was ejected. Additionally, a type-III radio burst was observed by both the STEREO-A and WIND spacecraft during the time of the first event, which means that at least some of the field lines were open. Furthermore, even in the scenario of large closed loops, the stopping distance along the jet body would remain the same, thus the conclusion of an additional particle acceleration site near the jet top (or loop apex) still holds, regardless of the jet geometry.

The HXR source to the north of the later jet appeared last among the three HXR sources, but still during a time when the jet was visible in EUV filters. It could possibly be related to the jet, since the formation of the jet would change the magnetic configuration of the active region, but it could also be a separate event. In the AIA 94 Å and 131 Å channels, a few compact loops brightened at the same time and location as the northern HXR source. If the energetic electrons at that northern location were originally from the jet base, neither the electron path nor the density along the path is clear. The typical coronal density for an active region is about 10<sup>9</sup> cm<sup>-3</sup> (e.g., Newkirk 1961), corresponding to a stopping distance of 200" for electrons of 10 keV. Thus, in general situations, energetic electrons could travel a decent distance in the corona, but it is also possible that the density in this active region is larger than

that typical value. Unfortunately, due to the lack of data, we could not determine which was the case for this source.

#### 4.3. Energy Budget

Investigating the partition of different energy components can help us to understand the energy release process in these events. Such calculations have been done in the past for a number of flares and CMEs (e.g., Emslie et al. 2012; Aschwanden et al. 2015; Warmuth & Mann 2016), but only for a few jets so far (Pucci et al. 2013). Here, we present our estimates of the various energy components for the later event, including kinetic energy, gravitational energy, thermal energy, and the energy in nonthermal electrons. We calculated the maximum amount of energy that could be converted into each of the forms above.

The jet's major eruption started from 20:46 UT, which was visible in all AIA filters and had a speed of  $\sim$ 260 km s<sup>-1</sup> (Figure 11). The density of this plasma was derived from its DEM, which is  $1.3 \times 10^{10}$  cm<sup>-3</sup>. Assuming the jet body that contained this group of plasma to be a cylinder (5" diameter and 15" height), the peak kinetic energy of the jet is  $5 \times 10^{26}$  erg.

The maximum height of this jet is  $\sim 80''$ ; however, as the height increases, the amount of plasma that travels there decreases, and it is not clear what fraction of plasma finally reaches the maximum height. Therefore, instead of calculating the maximum gravitational energy of the jet, we set an upper limit of  $2\times10^{26}$  erg, which is the gravitational energy if all the plasma of the major eruption reaches a height of 80''. This upper limit is smaller than the kinetic energy of the jet, which is consistent with our finding of freefall velocity in Section 4.1, and again means that the plasma motion is not ballistic. Similar results have been reported in a few other observations of EUV jets (Moschou et al. 2013), H-alpha surges (Roy 1973), and even coronal rains (Kohutova & Verwichte 2016).

The thermal energy is dominated by contributions from HXR sources. Using the joint DEMs, the peak thermal energy for each HXR source is about  $5 \times 10^{27}$  erg. This value is consistent with the flare thermal energies that are found for other jets in Musset et al. (2020).

The energy in nonthermal electrons can be simply estimated as  $E_{\rm nonth} = N_{\rm e} E_{e,\rm ave}$ , where  $N_e$  is the total number of accelerated electrons and  $E_{e,\rm ave}$  is the average electron energy. Adopting the thick-target approximation, and using the parameters from Table 1, the nonthermal energy for each HXR source is about  $(6-11)\times 10^{29}$  erg. However, this value is calculated based on RHESSI measurements. If we apply the cross-calibration factor between AIA and RHESSI, to match the calculations of the other energy forms, the nonthermal energy for each HXR source becomes  $(3-6)\times 10^{29}$  erg.

The energies of the HXR sources in this event can be compared to those in previous studies of flare energetics. Emslie et al. (2012) studied 38 eruptive events (all except one were M- or X-class flares, and most flares were accompanied by a CME), and they found that the flare thermal energies were always smaller than the energies in the accelerated particles. Similar results were found in a later study by Warmuth & Mann (2016), where the median ratio of thermal energies to nonthermal energies in the electrons for 24 (C-to-X class) flares was 0.3. In a subclass of "cold" flares (Lysenko et al. 2018), the thermal energy is equal (within the uncertainties) to the nonthermal energy deposition (Fleishman et al. 2016;

Motorina et al. 2020; Fleishman et al. 2021). (Theoretically, the thermal energy cannot be less than the nonthermal energy, as the nonthermal energy decays into the thermal energy.) For our jet event, which contains low-C-class flares, the thermal energies are more than one order of magnitude smaller than the nonthermal energies. Therefore, the conclusion that the nonthermal energy is always larger than or at least equal to the thermal energy is likely consistent across a wide range of flare classes, and regardless of whether the flare is associated with a jet/CME or not.

However, the energy partition between the jet and the associated flares is different from the energy partition between a CME and a flare. For this event, the kinetic/gravitational energy of the jet is more than one order of magnitude smaller than the energy of the flares (thermal/nonthermal), while in Emslie et al. (2012), the total energy of the CME is usually significantly larger—the kinetic energy in confined flares is much smaller (Fleishman et al. 2021), though. This variety could be explained in the minifilament eruption scenario, with jets and CMEs being parts of the same eruptive events, but with the energy partition changing with scale; or it could also indicate that there are fundamental differences between jets and CMEs. To further answer this question, future studies with more samples of flare-related jets are needed.

Finally, if the plasma filling factor is less than 1, then the kinetic energy, gravitational energy, and thermal energy should all be multiplied by the square root of the filling factor, while the nonthermal energy remains the same. However, this modification would not change the event energy partition significantly. Also, it should be noted that there are still other forms of energy that have not been considered in the calculations above, such as magnetic energy, wave energy, etc. These energies could also be important components of the event energy budget, but are hard to evaluate here, due to the limited data.

### 4.4. Comparison to the Current Jet Models

Considering the locations of the hot plasma as well as the HXR sources, these two jets are interesting examples to compare with current jet models. On the one hand, the source at the base of the jet is consistent with what is expected from jet models. During the minifilament eruption at the jet base, magnetic reconnection occurs close to the bottom of the corona, heating the plasma there directly and generating accelerated electrons near the reconnection site. The downward-traveling energetic electrons radiate bremsstrahlung emissions as they collide with the dense chromosphere, producing an HXR source and/or further heating the ambient plasma at the base of the jet. On the other hand, the processes after a jet's eruption are generally not considered by those models; thus, the hot plasma and the HXR source at the top of the jet are not expected. Our observations have shown that additional particle acceleration could occur at other locations besides the jet base. In other words, there could be multiple reconnection and energy release sites in a single jet event. Also, despite the significantly different particle acceleration sites (and even two separate events), the nonthermal electrons share very similar energy distributions. The spectral indices around 10 and the low-energy cutoffs around 9 keV suggest that jet reconnection typically produces only mild particle acceleration. These low-energy cutoffs are similar to those of the cold flares (e.g.,

Motorina et al. 2020), while the spectra are much softer in the case of the jets.

Another interesting point about these events is the relation between the hot and cool material. For both jets, the cool ejections observed in the 304 Å filter were adjacent to the hot ejections observed in the 94 Å and 131 Å filters. While past simulations have successfully produced a hot jet and a cool jet (or surge) in a single event, it is generally expected that hot and cool jets are driven through different mechanisms. For example, in the simulation by Yokoyama & Shibata (1996), the hot jet was accelerated by the pressure gradient, while the cool surge was accelerated by magnetic tension. Similarly, in an observational study by Matsui et al. (2012), the hot component (at coronal temperatures) was generated by chromospheric evaporation, while the cool component (at chromospheric temperatures) was accelerated by magnetic force. However, though the observation of the earlier jet does not conflict with this picture, the later jet had consistent velocities in hot and cool filters, indicating that some of the hot components might be driven by a very similar process as the cool components in that event. Therefore, at least in some cases, the hot and cool components must be more closely related, and a jet model should be able to explain this kind of observation, as well as those similar to Matsui et al. (2012).

### 5. Summary

In this paper, we present a multiwavelength analysis of two active-region jets that were associated with low-C-class flares on 2014 November 13. The key aspects of this study include the following:

- 1. In both events, hot (≥10MK) plasma not only appeared near the base of the jet (which is the location of the primary reconnection site) at the beginning, but also appeared near the top of the jet after a few minutes.
- 2. Four RHESSI HXR sources were observed: one (at the jet top) in the first event and three (at the jet base, jet top, and a location to the north of the jet) in the later event. All those sources showed evidence of mildly accelerated electrons which had spectral indices around 10 and extended to low energies around 9 keV.
- 3. Various jet velocities were identified through time—distance plots, including major upward velocities of ~250 km s<sup>-1</sup> and downward velocities of ~100 km s<sup>-1</sup>. Fast outflows of ~700 km s<sup>-1</sup> or ~400 km s<sup>-1</sup> were observed only in the hot AIA 131 Å filter at the beginning of each jet. These velocities indicate that the jets were likely driven by magnetic force.
- 4. The HXR source and hot plasma at the base of the jet were expected from current models. However, the HXR sources at the top of the jet were likely produced by energetic electrons that were accelerated very close to the top location, rather than electrons that were accelerated near the jet base but traveled to the top. This means that there was more than one reconnection and particle acceleration site in each event.

Coronal jets are an important form of solar activity involving particle acceleration, and they share similarities with larger eruptive events, such as CMEs. HXRs can provide important constraints on the hot plasma within a coronal jet, as well as unique diagnostics of energetic electron populations. To obtain the best constraints for jet models, observations should take

advantage of state-of-the-art instruments in different wavebands, but only a few studies have included HXR observations to date. In future work, we would like to extend the method described in this paper to other coronal jets. Those jets could come from the jet database that will be generated by the citizen science project Solar Jet Hunter<sup>6</sup> (which was launched through the Zooniverse platform in 2021 December). We expect studies with more jet samples to further advance our understanding of particle acceleration in jets.

Furthermore, as shown in this study, HXR sources that are associated with jets could be found in the corona, and they could be faint in some events, thus not identified by current instruments. One solution is to develop direct-focusing instruments, such as that demonstrated by the Focusing Optics X-ray Solar Imager sounding rocket experiment, which will provide better sensitivity and a better dynamic range for future HXR observations.

This work is supported by NASA Heliophysics Guest Investigator grant 80NSSC20K0718. Y.Z. is also supported by the NASA FINESST program 80NSSC21K1387. N.K.P. acknowledges support from NASA's SDO/AIA and HGI grants. We thank Samaiyah Farid for helpful discussions. We are also grateful to the SDO/AIA, RHESSI, Hinode/XRT, and IRIS teams for their open data policy. Hinode is a Japanese mission developed and launched by ISAS/JAXA, with NAOJ as domestic partner and NASA and STFC (UK) as international partners. It is operated by these agencies in cooperation with ESA and the NSC (Norway). IRIS is a NASA small explorer mission, developed and operated by LMSAL, with mission operations executed at the NASA Ames Research Center, and major contributions to downlink communications funded by ESA and the Norwegian Space Centre.

# **ORCID iDs**

Yixian Zhang https://orcid.org/0000-0001-8941-2017
Sophie Musset https://orcid.org/0000-0002-0945-8996
Lindsay Glesener https://orcid.org/0000-0001-7092-2703
Navdeep K. Panesar https://orcid.org/0000-0001-7620-362X
Gregory D. Fleishman https://orcid.org/0000-0001-5557-2100

### References

```
Adams, M., Sterling, A. C., Moore, R. L., & Gary, G. A. 2014, ApJ, 783, 11 Aschwanden, M. J. 2005, Physics of the Solar Corona (Berlin: Springer), 283 Aschwanden, M. J., Boerner, P., Ryan, D., et al. 2015, ApJ, 802, 53 Bain, H. M., & Fletcher, L. 2009, A&A, 508, 1443 Battaglia, M., & Kontar, E. P. 2013, ApJ, 779, 107 Chae, J., Qiu, J., Wang, H., & Goode, P. R. 1999, ApJL, 513, L75 Cirtain, J. W., Golub, L., Lundquist, L., et al. 2007, Sci, 318, 1580 Doschek, G. A., Warren, H. P., & Young, P. R. 2013, ApJ, 767, 55 Emslie, A. G., Dennis, B. R., Shih, A. Y., et al. 2012, ApJ, 759, 71 Fisher, G. H., Canfield, R. C., & McClymont, A. N. 1984, ApJL, 281, L79 Fleishman, G. D., Kleint, L., Motorina, G. G., Nita, G. M., & Kontar, E. P. 2021, ApJ, 913, 97
```

```
Fleishman, G. D., Nita, G. M., Chen, B., Yu, S., & Gary, D. E. 2022, Natur,
  606, 674
Fleishman, G. D., Pal'shin, V. D., Meshalkina, N., et al. 2016, ApJ, 822, 71
Glesener, L., & Fleishman, G. D. 2018, ApJ, 867, 84
Glesener, L., Krucker, S., & Lin, R. P. 2012, ApJ, 754, 9
Hannah, I. G., Christe, S., Krucker, S., et al. 2008, ApJ, 677, 704
Hannah, I. G., & Kontar, E. P. 2012, A&A, 539, A146
Hannah, I. G., & Kontar, E. P. 2013, A&A, 553, A10
Hong, J., Jiang, Y., Zheng, R., et al. 2011, ApJL, 738, L20
Huang, Z., Madjarska, M. S., Doyle, J. G., & Lamb, D. A. 2012, A&A,
Innes, D. E., Inhester, B., Axford, W. I., & Wilhelm, K. 1997, Natur, 386, 811
Kohutova, P., & Verwichte, E. 2016, ApJ, 827, 39
Krucker, S., Battaglia, M., Cargill, P. J., et al. 2008, A&ARv, 16, 155
Krucker, S., Kontar, E. P., Christe, S., Glesener, L., & Lin, R. P. 2011, ApJ,
  742, 82
Lemen, J. R., Title, A. M., Akin, D. J., et al. 2012, SoPh, 275, 17
Lin, R. P., Dennis, B. R., Hurford, G. J., et al. 2002, SoPh, 210, 3
Lysenko, A. L., Altyntsev, A. T., Meshalkina, N. S., Zhdanov, D., &
  Fleishman, G. D. 2018, ApJ, 856, 111
Matsui, Y., Yokoyama, T., Kitagawa, N., & Imada, S. 2012, ApJ, 759, 15
McGlasson, R. A., Panesar, N. K., Sterling, A. C., & Moore, R. L. 2019, ApJ,
  882, 16
Moore, R. L., Cirtain, J. W., Sterling, A. C., & Falconer, D. A. 2010, ApJ,
  720, 757
Moore, R. L., Sterling, A. C., Falconer, D. A., & Robe, D. 2013, ApJ, 769, 134
Moore, R. L., Sterling, A. C., & Panesar, N. K. 2018, ApJ, 859, 3
Moschou, S. P., Tsinganos, K., Vourlidas, A., & Archontis, V. 2013, SoPh,
Motorina, G. G., Fleishman, G. D., & Kontar, E. P. 2020, ApJ, 890, 75
Muglach, K. 2021, ApJ, 909, 133
Mulay, S. M., Tripathi, D., Zanna, G. D., & Mason, H. 2016, A&A, 589, A79
Musset, S., Jeunon, M., & Glesener, L. 2020, ApJ, 889, 183
Newkirk, G. 1961, ApJ, 133, 983
Nisticò, G., Bothmer, V., Patsourakos, S., & Zimbardo, G. 2009, SoPh, 259, 87
Panesar, N. K., Sterling, A. C., & Moore, R. L. 2016a, ApJL, 822, L23
Panesar, N. K., Sterling, A. C., Moore, R. L., & Chakrapani, P. 2016b, ApJL,
  832, L7
Panesar, N. K., Sterling, A. C., & Moore, R. L. 2017, ApJ, 844, 131
Panesar, N. K., Sterling, A. C., & Moore, R. L. 2018, ApJ, 853, 189
Pariat, E., Dalmasse, K., DeVore, C. R., Antiochos, S. K., & Karpen, J. T.
  2015, A&A, 573, A130
Pariat, E., Dalmasse, K., DeVore, C. R., Antiochos, S. K., & Karpen, J. T.
  2016, A&A, 596, A36
Pucci, S., Poletto, G., Sterling, A. C., & Romoli, M. 2013, ApJ, 776, 16
Raouafi, N. E., Patsourakos, S., Pariat, E., et al. 2016, SSRv, 201, 1
Roy, J. R. 1973, SoPh, 32, 139
Sadykov, V. M., Dominguez, S. V., Kosovichev, A. G., et al. 2015, ApJ,
  805, 167
Savcheva, A., Cirtain, J., DeLuca, E. E., et al. 2007, PASJ, 59, S771
Schmelz, J. T., Asgari-Targhi, M., Christian, G. M., Dhaliwal, R. S., &
  Pathak, S. 2015, ApJ, 806, 232
Schmelz, J. T., Kashyap, V. L., Saar, S. H., et al. 2009, ApJ, 704, 863
                   SA, 477, 217
Shen, Y. 2021, RSP
Shibata, K., Ishido, Y., Acton, L. W., et al. 1992, PASJ, 44, L173
Shimojo, M., Hashimoto, S., Shibata, K., et al. 1996, PASJ, 48, 123
Sterling, A. C., Moore, R. L., Falconer, D. A., & Adams, M. 2015, Natur,
  523, 437
Sterling, A. C., Moore, R. L., Falconer, D. A., et al. 2016, ApJ, 821, 100
Tian, H., Young, P. R., Reeves, K. K., et al. 2015, ApJ, 811, 139
Warmuth, A., & Mann, G. 2016, A&A, 588, A116
Wright, P. J., Hannah, I. G., Grefenstette, B. W., et al. 2017, ApJ, 844, 132
Wyper, P. F., Antiochos, S. K., & DeVore, C. R. 2017, Natur, 544, 452
Wyper, P. F., DeVore, C. R., & Antiochos, S. K. 2018, ApJ, 852, 98
Yokoyama, T., & Shibata, K. 1995, Natur, 375, 42
Yokoyama, T., & Shibata, K. 1996, PASJ, 48, 353
```

https://www.zooniverse.org/projects/sophiemu/solar-jet-hunter